Digital Current-Control Schemes

© ARTVILLE

LEONARDO RODRIGUES LIMONGI,
RADU BOJOI,
GIOVANNI GRIVA,
and ALBERTO TENCONI

Comparing the Performance of Digital Signal Processor-Based Current Controllers for Three-Phase Active Power Filters

Digital Current-Control Schemes

Digital Object Identifier 10.1109/MIE.2009.931894

The wide use of nonlinear loads, such as front-end rectifiers connected to the power distribution systems for dc supply or inverter-based applications, causes significant power quality degradation in power distribution networks in terms of current/voltage harmonics, power factor, and resonance problems. Passive LC filters (together with capacitor banks for reactive power compensation) are simple, low-cost, and high-efficiency solutions. However, their performance strongly depends on the source impedance and can lead to unwanted resonance phenomena with the network [1]. In addition, passive solutions are not effective for applications in which the nonlinear load exhibits fast transients.

During the last decade, the reduced cost and increased reliability of power electronics and digital signal processor (DSP) technology have driven new interest in active filtering. In the case there are nonlinear current-source loads, the shunt active power filter (APF) is considered an effective solution for reducing the current harmonics for low to medium power applications [1]–[5]. Active filtering is advantageous where a fast response to dynamic load changes is required [5]. In addition, the shunt APF represents a versatile power-conditioning tool since it is able to compensate the load reactive power and the load imbalances.

The basic compensation scheme for a plant with a current-type nonlinear load using a shunt APF is shown in Figure 1. The APF is a three-phase voltage-source inverter (VSI) that has only a large capacitor on its dc link. The inverter is connected to the load at the point of common coupling (PCC) through an input inductor.

The APF operates as a controlled current source generating the load harmonic currents $\Sigma_{h\neq 1} i_h$ (Figure 1). As a result, the current drawn from the mains at the PCC will be sinusoidal. The APF will need an active fundamental current component i_{APF_1} to keep its dc-link capacitor charged at a voltage higher than the peak line-to-line voltage (to have enough voltage margin to control the currents that must be injected at the PCC). Since the APF reference currents are not sinusoidal, obtaining zero steady-state error is a challenging task.

In addition, the load input inductor (Figure 1) is usually designed for a voltage drop of less than 5% of the mains voltage at rated current. As a consequence, for high-power loads, the load currents have high di/dt values, requiring very high slope variations of the reference currents. Thus, a key issue in APF control is the current-control strategy.

Since the performances of all the current controllers are rather similar, choosing the best solution should be strongly influenced by the ease of implementation and the execution time.

During the last two decades, different current-control solutions for active power filters [6]–[22] have been reported in the literature. The use of proportional-integral (PI) controllers is a simple and well-known solution that is effective only if the reference currents are dc signals. For the case in which the reference currents are sinusoidal at the fundamental frequency (as happens for pulse width modulation (PWM) boost rectifiers, for example), the PI control is usually implemented in a rotating (synchronous) (d, q) reference frame aligned with the PCC voltage vector. In this case, the actual and the reference currents are dc signals for steady-state operation. For APFs, though, the fundamental components of the reference current (the active component to keep the dc-link capacitor charged and the reactive component for reactive power compensation) are dc values in the (d, q) synchronous reference frame aligned with the PCC voltage vector, but the reference components for harmonic compensation are oscillating components (far from dc signals) [2]. Therefore, the PI control cannot adequately track current references and results in steady-state error due to the finite controller gain. For

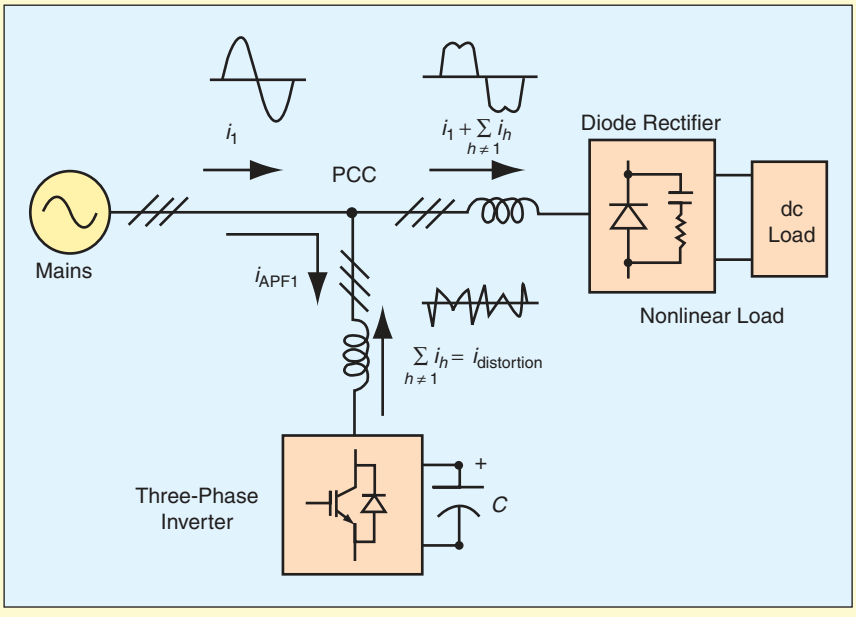

FIGURE 1 – Basic current harmonic compensation scheme of a nonlinear load using a shunt APF.

this reason, PI controllers are not suitable for active power filters unless the switching frequency is high enough to yield a satisfactory controller bandwidth [2].

High controller bandwidth is easily achievable by using nonlinear regulators, such as hysteresis controllers [7]. The major drawback of this solution, however, is that a variable switching frequency is obtained. A constant switching frequency can be achieved with adaptive algorithms, but a digital implementation would require field-programmable gate array (FPGA)-based digital systems. Here, we focus only on DSP-based solutions.

The dead-beat (DB) schemes (sometimes featuring predictive algorithms) [9]–[12] operate with constant APF switching frequency and are computationally effective. Nevertheless, the DB schemes are quite sensitive to parameter detuning and to the inverter dead-time effects that must be properly compensated.

On the other hand, the current-control solutions based on selective harmonic compensation schemes (also known as frequency-selective schemes) [13]–[22] have proved to be very interesting in terms of performance, with acceptable computational requirements for industrial applications using up-to-date fixed-point DSPs [21]. These methods can be applied when the harmonic spectrum of the distortion current $i_{\text{distortion}}$ (Figure 1) to be compensated consists of harmonics that have well-known orders and sequences. When the load is supplied through a three-phase diode or thyristor front-end rectifiers, these harmonics are of order $h = 6k \pm 1$ ($k = 1, 2, \ldots$) of the fundamental frequency [13]. If we consider the fundamental frequency component as a positive-type sequence, the corresponding sequence representations of the current harmonics in stationary and synchronous reference frames are illustrated in Table 1. Thus, it is possible to identify specific undesired harmonic currents, which are independently compensated according to a control scheme that has a modular structure depending on the preselected harmonics to be compensated [13].

By comparing the performance of different digital, DSP-based current-control techniques for shunt APFs requiring high-performance current control in applications with fast transients, we hoped to identify the most promising solution for an industrial implementation.

The current-control schemes implemented for the comparison were the following:

- PI controller in a synchronous reference frame (PI-SRF) [2]
- DB controller implemented in a stationary reference frame [9]–[12]
- PI controller in a synchronous reference frame with multiple rotating integrators (PI-MRI) [14]
- stationary frame controller with proportional regulator and sinusoidal signal integrators (P-SSI) [19]
- P-SSI controller with multiple SSIs in a synchronous reference frame (P-SSI-SRF) [21]
- PI controller with resonant regulators (PI-RES) in a synchronous reference frame [22]
- repetitive control [20].

The current-control solutions were compared through simulations and experimental tests for a 25-kVA APF prototype using the same switching frequency and control tasks (excepting current control). In the case of current-control solutions based on selective harmonic compensation schemes, the harmonics were compensated up to the 25th harmonic of the load current (1,250 Hz). The main criteria for performance evaluation are the total harmonic distortion (THD) of the mains line current and the transient performance for fast load variations. In addition, the computational burden and design complexity for a 16-b fixed-point DSP were also evaluated.

TABLE 1—CURRENT HARMONICS FOR THREE-PHASE RECTIFIERS.

HARMONIC IN (α, β) STATIONARY REFERENCE FRAME	SEQUENCE	HARMONIC ORDER IN (d, q) SYNCHRONOUS REFERENCE FRAME ROTATING AT FUNDAMENTAL FREQUENCY
1 (Fundamental)	Positive	dc
5	Negative	6
7	Positive	6
....	....	....
$6 \cdot k - 1$	Negative	$6 \cdot k$
$6 \cdot k + 1$	Positive	$6 \cdot k$

PI-SRF Controller

This current control is implemented in a (d, q) synchronous reference frame usually aligned with the PCC voltage vector. The basic scheme of the PI-SRF controller, shown in Figure 2(a), should include decoupling and feedforward terms to improve the controller performance [6] since the reference components for harmonic compensation are oscillating components in a (d, q) synchronous reference frame. Zero steady-state error can be achieved only if the APF switching frequency is high enough to yield a satisfactory controller bandwidth [2].

DB Controller

In a DB controller, the control algorithm calculates the APF phase voltage command to cancel the current error at the end of the following sampling period [9]–[12]. The control algorithm, which ensures a DB response for the first-order system modeling on the APF input inductance L_F, is [9]

$$\begin{aligned} v^*_{F,\alpha\beta}(k) = {} & 4v_{\alpha\beta}(k-1) - 2v_{\alpha\beta}(k-2) \\ & - v^*_{F,\alpha\beta}(k-1) + \frac{L_F}{T_s} \\ & \times [3i^*_{F,\alpha\beta}(k-1) \\ & - 2i^*_{F,\alpha\beta}(k-2) - i_{F,\alpha\beta}(k-1)] \end{aligned} \tag{1}$$

where k is the sampling instant and T_s is the sampling period. The other variables in this expression, represented in stationary (α, β) frame, are: the inverter output reference voltage components ($v^*_{F,\alpha\beta}$), the PCC voltage components ($v_{\alpha\beta}$), the filter current

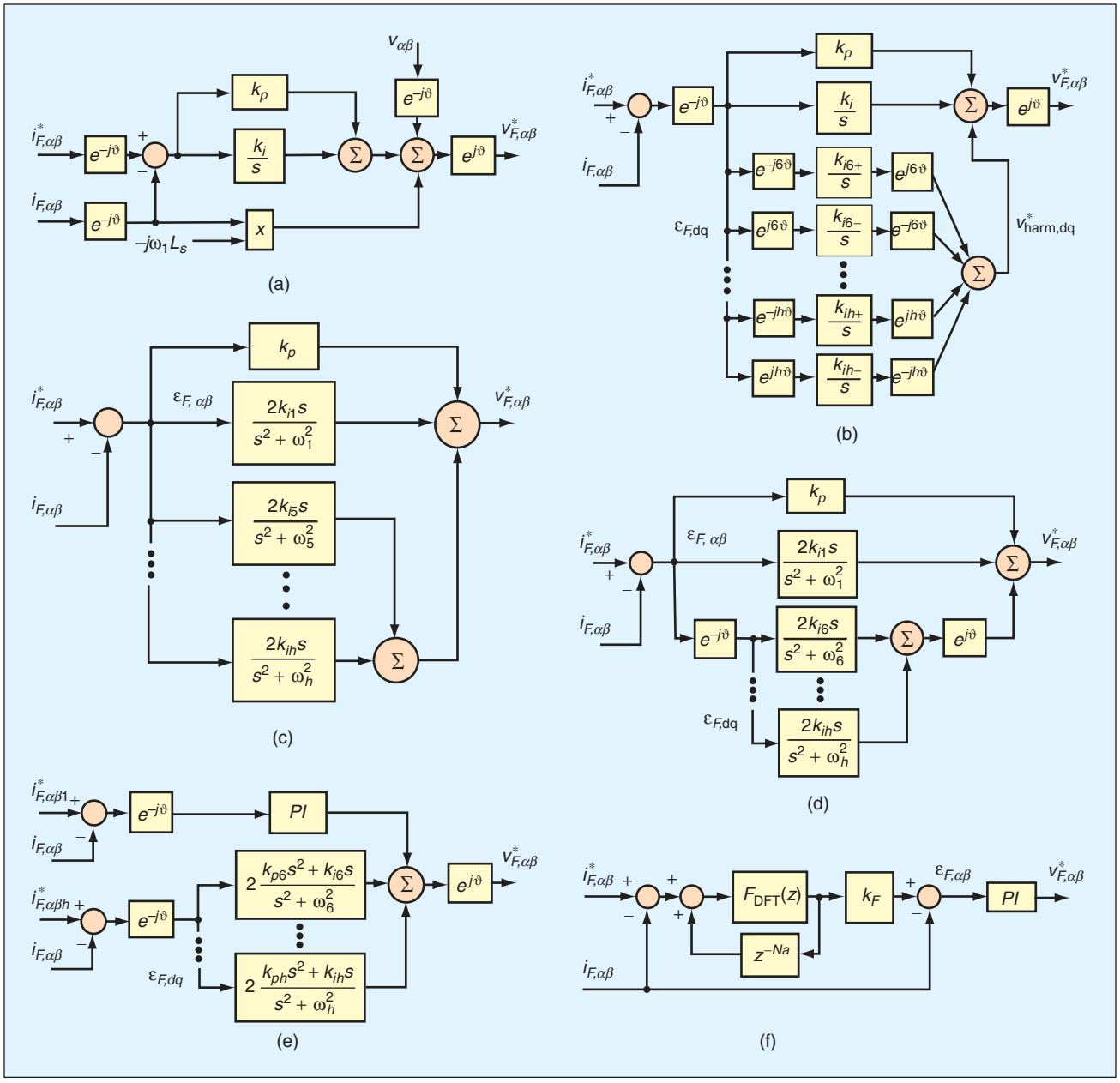

FIGURE 2 – Current controllers: (a) PI-SRF controller scheme, (b) PI-MRI controller with $h = 6k$ ($k = 1, 2, \ldots$), (c) P-SSI controller in stationary reference frame with $h = (6k \pm 1)$, ($k = 1, 2, \ldots$), (d) P-SSI with multiple SSIs in synchronous reference frame with $h = 6k$, ($k = 1, 2, ..$), (e) PI-RES controller scheme with $h = 6k$ ($k = 1, 2, ..$), and (f) repetitive control scheme.

reference components ($i^*_{F,\alpha\beta}$), and the filter current components ($i_{F,\alpha\beta}$). The main drawback of this method is related to the inaccuracy of the system parameters. In addition, the inverter nonlinear operation, due to the dead-time effects, must be taken into account.

PI-MRI Controller

If the current reference generation is implemented in a stationary reference frame, a possible solution for selective harmonic compensation is to use pure integrators operating in reference frames rotating at $(6k \pm 1)\omega_1$, $(k = 1, 2, \ldots)$ with proper sequence, i.e., $-5\omega_1$, $+7\omega_1$, $-11\omega_1$, $13\omega_1$, etc. [13]. If the current reference generation is implemented in the synchronous reference frame (d, q) rotating at the fundamental frequency ω_1, it is more convenient to use the integrators in multiple synchronous reference frames rotating at $\pm h\omega_1$, ($h = 6k$, $k = 1, 2, \ldots$) [14] [Figure 2(b)]. This array of integrators has as input the current error $\varepsilon_{F,dq}$ obtained in a (d, q) synchronous reference frame (aligned with the PCC voltage vector). A PI controller is used for the fundamental current component regulation to keep the APF dc-link capacitor charged and for reactive power compensation. In the case that there are unbalanced loads, a fundamental negative sequence PI regulator [not present in Figure 2(b)] should be added. This frequency selective algorithm requires multiple rotational transformations to individually compensate each harmonic. Due to the delay introduced by the sampling time, the PI-MRI controller becomes unstable

for the harmonics of high order. For this reason, an additional compensation angle ϑ_{ch} must be included in the inverse rotational transformation from the harmonic reference frame back to the synchronous reference frame, as shown in Figure 3. Considering the experimental tests performed for our comparison, best results are obtained if the compensation angle corresponds to two sampling periods T_s, i.e.,:

$$\vartheta_{ch} = 2h\omega_1 T_s, \;\; h = 6k \; (k = 1, 2, \ldots). \tag{2}$$

P-SSI Controller

To eliminate the need of multiple rotating reference frames, a P-SSI controller [Figure 2(c)] [17], [19] is based on the SSI [19], which guarantees that the actual current tracks its sinusoidal reference (with zero steady-state error) and is tuned on a specified frequency ω_0. In the continuous time domain, the transfer function of a P-SSI controller is [19]

$$H_{P-SSI} = k_p + \frac{2k_i s}{s^2+\omega_0^2} = H_P(s)+H_{SSI}(s) \tag{3}$$

where k_p is the proportional gain, k_i is the integral gain, and ω_0 is the resonance frequency. Using SSI regulators provides a number of advantages.

- There is zero steady-state error for signals having the same frequency as ω_0.
- Multiple SSIs with different resonance frequencies can operate in parallel without interfering with each other since an SSI acts as a resonant filter, tuned on its resonance frequency ω_0.
- An SSI can operate with both positive and negative sequence signals since an SSI is equivalent to two integrators rotating at $\pm\omega_0$.

Using the concept of frequency-selective compensation, a P-SSI controller for an APF [Figure 2(c)] uses multiple SSIs in a stationary reference frame, tuned on selected current harmonics of order $(6k \pm 1)$, $(k = 1, 2, \ldots)$ [19]. For the fundamental current component, a P-SSI regulator tuned on the fundamental frequency is used. Its main function is to control both the active current component needed to keep the dc-link capacitor charged at a specified voltage and the reactive current component for reactive power compensation. Unbalanced load compensation also can be implemented [19] since SSI regulators are able to deal with both positive and negative current sequence components. The block diagram used for one SSI in our comparison is shown in Figure 4. The state-space model that corresponds to Figure 4 is [21]

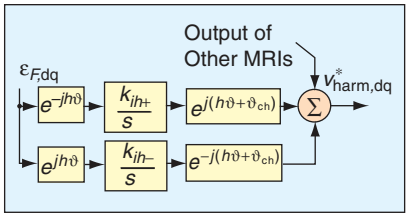

FIGURE 3 – Modified inverse rotational transformation from harmonic frame to (*d, q*) synchronous reference frame for the PI-MRI controller.

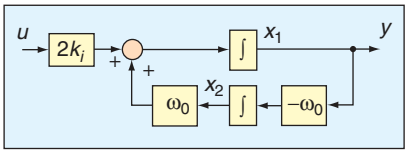

FIGURE 4 – Block diagram for an SSI having ω_0 as resonant frequency.

$$\begin{cases} \dfrac{d}{dt}[x] = [A]\cdot[x]+[B]\cdot u \\ \quad y = [C]\cdot[x] \end{cases} \tag{4}$$

where

$$[x] = \begin{bmatrix} x_1 \\ x_2 \end{bmatrix}, \quad [A] = \begin{bmatrix} 0 & \omega_0 \\ -\omega_0 & 0 \end{bmatrix},$$

$$[B] = \begin{bmatrix} 2k_i \\ 0 \end{bmatrix}, \quad [C] = [1 \;\; 0].$$

The discrete form of (4) is given as follows:

$$\begin{cases} [x(k+1)] = [A_d]\cdot[x(k)]+[B_d]\cdot u(k) \\ \quad y(k) = x_1(k) \end{cases} \tag{5}$$

$$[A_d] = \begin{bmatrix} \cos\delta & \sin\delta \\ -\sin\delta & \cos\delta \end{bmatrix},$$

$$[B_d] = \frac{2k_i}{\omega_0}\cdot\begin{bmatrix} \sin\delta \\ \cos\delta - 1 \end{bmatrix}, \text{ and } \delta = \omega_0 T_s$$

where T_s is the sampling time.

The delay caused by the sampling period causes SSI stability loss for large values of the resonance frequency ω_0. For this reason, a delay compensation scheme must be implemented. We have used the compensation scheme described in [21]: According to (3)–(5), the regulator states x_1 and x_2 are sinusoidal in steady-state conditions, having the same amplitude and being phase-shifted by 90 electrical degrees; for this reason, the compensation of the computation delay can be easily performed using the rotational transformation given by

$$y = [C]\cdot\begin{bmatrix} \cos(\omega_0\cdot kT_s) & 0 \\ 0 & \sin(\omega_0\cdot kT_s) \end{bmatrix}\cdot\begin{bmatrix} x_1 \\ x_2 \end{bmatrix} \tag{6}$$

where $k \geq 1$ is the number of sampling intervals to be compensated. Considering the experimental tests performed for our comparison, best results are obtained with $k = 2$. Another discrete form for SSIs with two sampling time delay compensation can be found in [19]. The control scheme of Figure 2(c) has the advantage of not requiring rotational transformations, but many SSIs might be necessary to reach the required THD performance, making digital implementations computationally heavier than with a PI-MRI controller.

P-SSI-SRF Controller

Using the SSI property of operating on both positive and negative sequence signals, the P-SSI-SRF controller uses multiple SSI regulators, as shown in Figure 2(d). One regulator, for the fundamental current component, is implemented in the stationary reference frame. The other regulators, for the current harmonics, are all implemented in a synchronous reference frame rotating at the fundamental frequency [21] and are tuned at $6k\omega_1$, $(k = 1, 2, \ldots)$. In fact, each SSI is equivalent to two integrators rotating

at $\pm h\omega_1$. This allows simultaneous compensation of two current harmonics with just one regulator and requires half the number of SSIs that are needed with the P-SSI controller. Implementations of P-SSI-SRF controllers on a 16-b fixed-point DSP are reported in [5] and [21].

PI-RES Controller

This solution [Figure 2(e)] is a derivation of the P-SSI-SRF controller and uses the same idea of the simultaneous compensation of two current harmonics with one regulator. The PI-RES employs resonant regulators that are equivalent to two complex PI regulators rotating at $\pm\omega_0$ [22]. In the continuous time domain, the transfer function of these resonant regulators is

$$H_{\mathrm{PI-RES}} = 2\frac{k_p s^2 + k_i s}{s^2 + \omega_0^2} \qquad (7)$$

where k_p is the proportional gain, k_i is the integral gain, and ω_0 is the resonance frequency. In the PI-RES, the reference current $i^*_{F,\alpha\beta}$ has two components: $i^*_{F,\alpha\beta 1}$ for fundamental frequency control and $i^*_{F,\alpha\beta h}$ for harmonic control [22]. For fundamental frequency control, a PI with a decoupling scheme [not shown in Figure 2(e)] is used. For the harmonic control, the parameters of each resonant controller are calculated using the pole-zero cancellation technique for each frequency of interest. Thus, each resonant controller is equivalent to two PI controllers rotating at $\pm h\omega_1$ having decoupled d and q axes. This results in an increase in the stability of the loop, avoiding delay compensation methods used for the previous techniques [22].

Repetitive Control

This current-control strategy uses a repetitive-based controller along with a simple P (or PI) controller, as shown in Figure 2(f). The repetitive controller uses a discrete Fourier transform (DFT), which has a frequency response approximately equal to the frequency response of the sum of SSIs used in the P-SSI control shown in Figure 2(c) [20]. The discrete transfer function of this DFT, which allows the implementation of the repetitive control with 100 taps for 10 kHz of switching frequency, is given by

$$F_{\mathrm{DFT}}(z) = \frac{2}{N}\sum_{i=0}^{N-1}\left(\sum_{k\epsilon N_h}\cos\left(\frac{\pi}{N}h(i+N_a)\right)\right)z^{-i} \qquad (8)$$

where N is the number of taps, N_h is the set of selected harmonic frequencies, and N_a is the number of leading steps necessary to maintain the system stability [20]. Therefore, using (8) makes it possible to implement all the SSI filters of Figure 2(c) using only this DFT of N coefficients in which the number of compensated harmonics is independent of N. This DFT filter can also be seen as a finite impulse response (FIR) filter [20].

The structure of the repetitive control is shown in Figure 2(f). This scheme was originally proposed in [20] using a feedback loop detecting

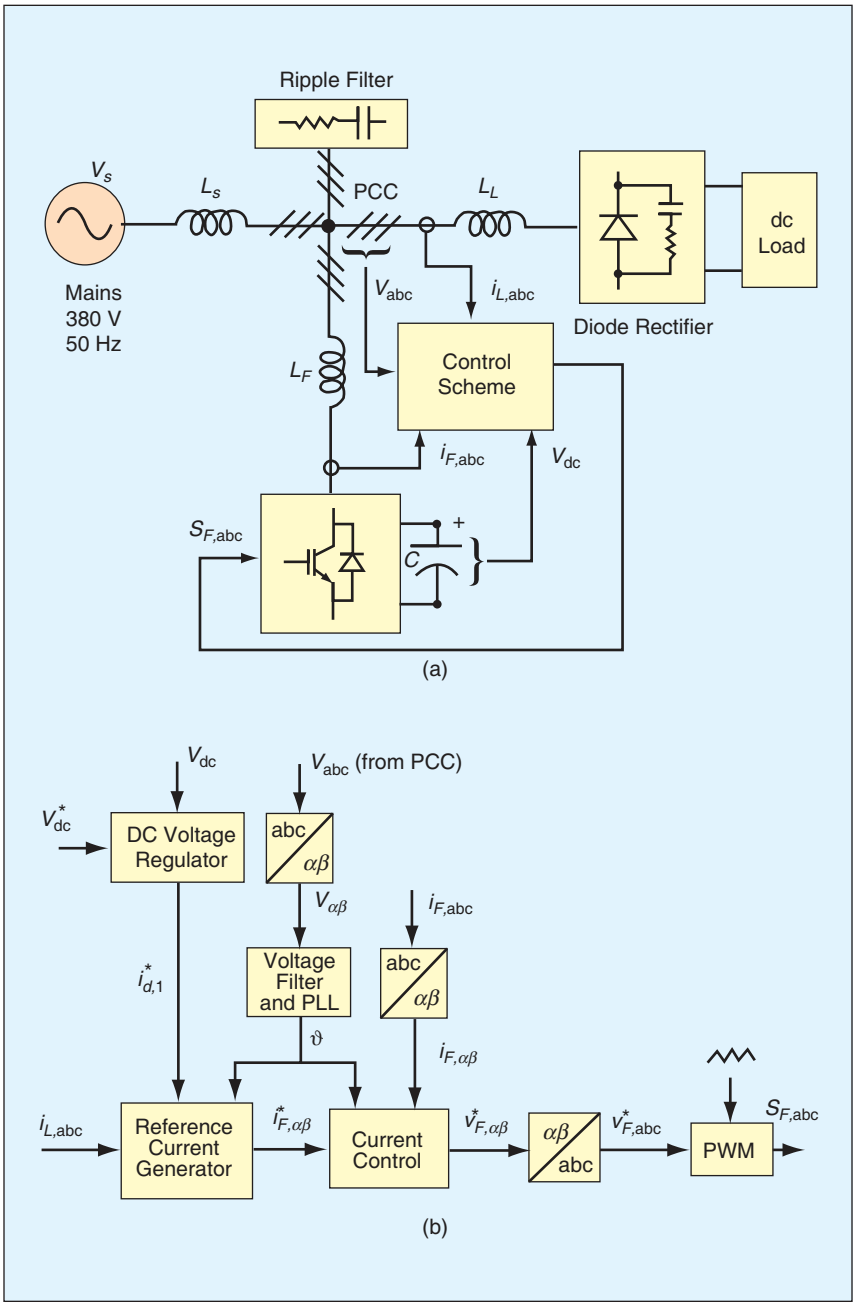

FIGURE 5 – APF scheme and control system: (a) APF test layout scheme and (b) block diagram of the whole APF control system.

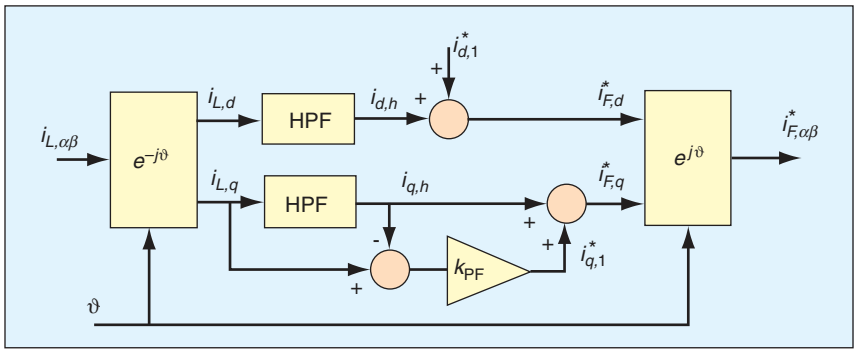

FIGURE 6 – APF reference current generation scheme.

the harmonic current at the source side. In our comparison, the repetitive control is implemented using a feedforward loop detecting the harmonic current at the load side. The difference between the two approaches does not change the performance of the current control. Following the scheme of Figure 2(f), the error signal is calculated from $i^*_{F,\alpha\beta}$ and $i_{F,\alpha\beta}$; after that, the DFT defined in (8) is used for precise tracking of the selected frequencies. A delay of N_a steps is then needed in the feedback path to recover zero phase shift of the loop $(F_{\mathrm{DFT}}(z)\cdot z^{-Na})$ at the desired frequencies. Also, the parameter K_F determines the controller speed response. The output of this scheme gives the reference currents for the current control [20].

Overall System Description

The current-control strategies were included in a digital control scheme for an APF that compensates the harmonics generated by a diode front-end rectifier, as shown in Figure 5(a). The quantities measured from the system were: the load currents $i_{L,\,abc}$, the APF currents $i_{F,\,abcs}$, the PCC line-to-line voltages v_{abc}, and the APF dc-link voltage v_{dc}. The current control block receives as inputs the APF reference and measured currents in the stationary (α, β) reference frame, as well as the position of the PCC voltage vector computed by means of a phase-locked loop (PLL) scheme [21]. The block diagram of the APF control scheme, shown in Figure 5(b), contains two

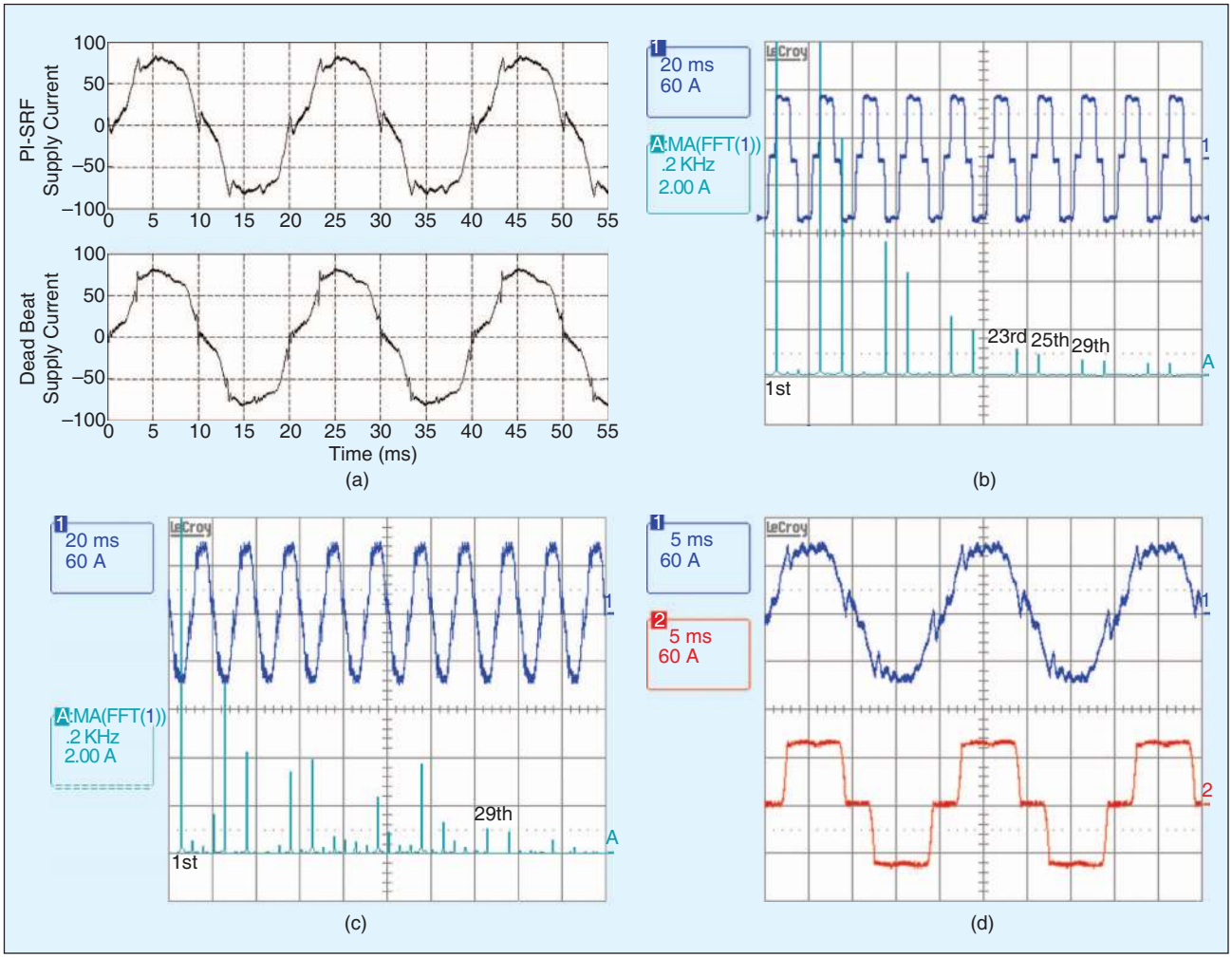

FIGURE 7 – Simulation and experimental results for PI-SRF and DB current controllers. (a) Simulation results. Mains current at steady-state operation for the APF using the PI-SRF and DB controllers. (b) Fourier analysis of the load current. (c) Fourier analysis of the mains current of the PI-SRF controller. (d) Mains current and load current for steady-state operation of the PI-SRF controller. Trace 1: i_{Sa} (A). Trace 2: i_{La} (A).

control loops: the dc voltage control loop and the APF current control loop. The dc voltage control loop is an outer loop that uses a simple PI regulator, and its output is the active current reference needed to keep the dc-link charged at the required value. The current control loop regulates the APF currents $i_{F,\,\alpha\beta}$ using one of the current-control schemes we've presented. The APF current reference $i^*_{F,\,\alpha\beta}$ is computed from the load currents $i_{L,\,\mathrm{abc}}$ and from the output of the dc-link regulator $i^*_{d,\,1}$, as shown in Figure 5(b). The reference generator scheme [21], shown in Figure 6, is implemented in the $(d,\ q)$ reference frame aligned with the PCC voltage vector. The harmonics to be compensated are extracted by means of high-pass filters. The fundamental reactive reference component $i^*_{q,\,1}$ is computed from the dc value of the q–axis load current component by means of the gain k_{PF}, according to the desired power factor compensation strategy. This reference current generator is described in detail in [21].

Simulation and Experimental Results

We compared the current-control solutions we've presented using simulations and experimental tests on a 25-kVA APF prototype [Figure 5(a)] compensating a 50-kVA nonlinear load. The APF switching frequency is 10 kHz. The dc-link reference voltage of the insulated gate bipolar transistor (IGBT) inverter is set at 730 V. The inverter interface inductance, L_F, and the input load inductance, L_L, are equal to 250 μH. The total estimated mains inductance, L_S, is about 120 μH. The whole APF control scheme [Figure 5(b)] is implemented on the dSPACE DS1103 development board. To guarantee the same conditions for comparison, this scheme was used for all the current-control techniques previously described. Also, all the control strategies were implemented with the same switching frequency, and the harmonics for frequency-selective techniques were compensated up to the 25th load current harmonic (1,250 Hz). The parameters of all the current-control schemes tested were

- PI-SRF: $k_p = 1.4$, $k_i = 4{,}000$
- PI-MRI: $k_p = 1.4$, $k_i = 200$, $k_{i6+} = 150$, $k_{i6-} = 150$, $k_{i12+} = 80$, $k_{i12-} = 80$, $k_{i18+} = 80$, $k_{i18-} = 80$, $k_{i24+} = 50$, $k_{i24-} = 50$
- P-SSI: $k_p = 1.4$, $k_{i1} = 200$, $k_{i5} = 150$, $k_{i7} = 150$, $k_{i11} = 80$, $k_{i13} = 80$, $k_{i17} = 80$, $k_{i19} = 80$, $k_{i23} = 50$, $k_{i25} = 50$
- P-SSI-SRF: $k_p = 1.4$, $k_{i1} = 200$, $k_{i6} = 150$, $k_{i12} = 80$, $k_{i18} = 80$, $k_{i24} = 50$
- PI-RES: $k_p = 0.5$, $k_i = 200$, $k_{p6} = 0.2$, $k_{p12} = 0.1$, $k_{p18} = 0.1$, $k_{p24} = 0.05$, $k_{i6} = 20$, $k_{i12} = 10$, $k_{i18} = 10$, $k_{i24} = 5$
- repetitive control: $k_p = 1.4$, $k_{i1} = 200$, $N = 100$, $N_a = 3$, $k_F = 1$.

TABLE 2—STEADY-STATE PERFORMANCE OF CURRENT CONTROLLERS.

CURRENT CONTROL	THD OF MAINS CURRENT COMPUTED UP TO THE 50TH HARMONIC
PI-MRI	2.51%
P-SSI	2.59%
P-SSI-SRF	2.57%
PI-RES	2.59%
Repetitive	2.42%

It is important to note that all parameters were set to be equivalent to guarantee a fair comparison. For example, all proportional gains are equal; in the case of PI-RES current control, the equivalent proportional constant is $(k_p + \Sigma_h 2k_{\mathrm{ph}})$. The same equivalence is also valid for the integral gains of the multiple rotating integrators and sinusoidal integrators.

The source voltages for the experimental tests are balanced and distorted by the nonlinear load. It must be emphasized that the influence of the source voltages is important for the detection of the PCC voltage vector position ϑ, with direct influence on the current reference computation. The PLL used for the experimental tests is described in detail in [21]. It is able to obtain a smooth PCC voltage vector position even under highly distorted PCC voltages [5], so the current-control schemes should practically not be influenced by the PCC voltage distortion, making their comparison easier.

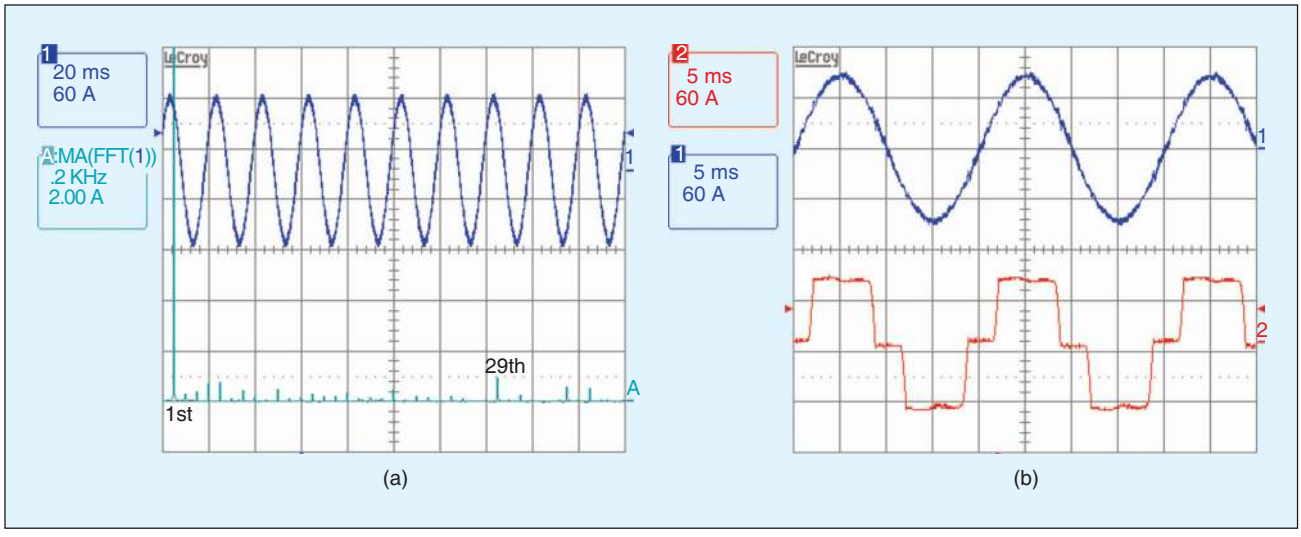

FIGURE 8 – Experimental results for the PI-MRI controller: (a) Fourier analysis of the mains current and (b) Mains current and load current for steady-state operation. Trace 1: i_{Sa} (A). Trace 2: i_{La} (A).

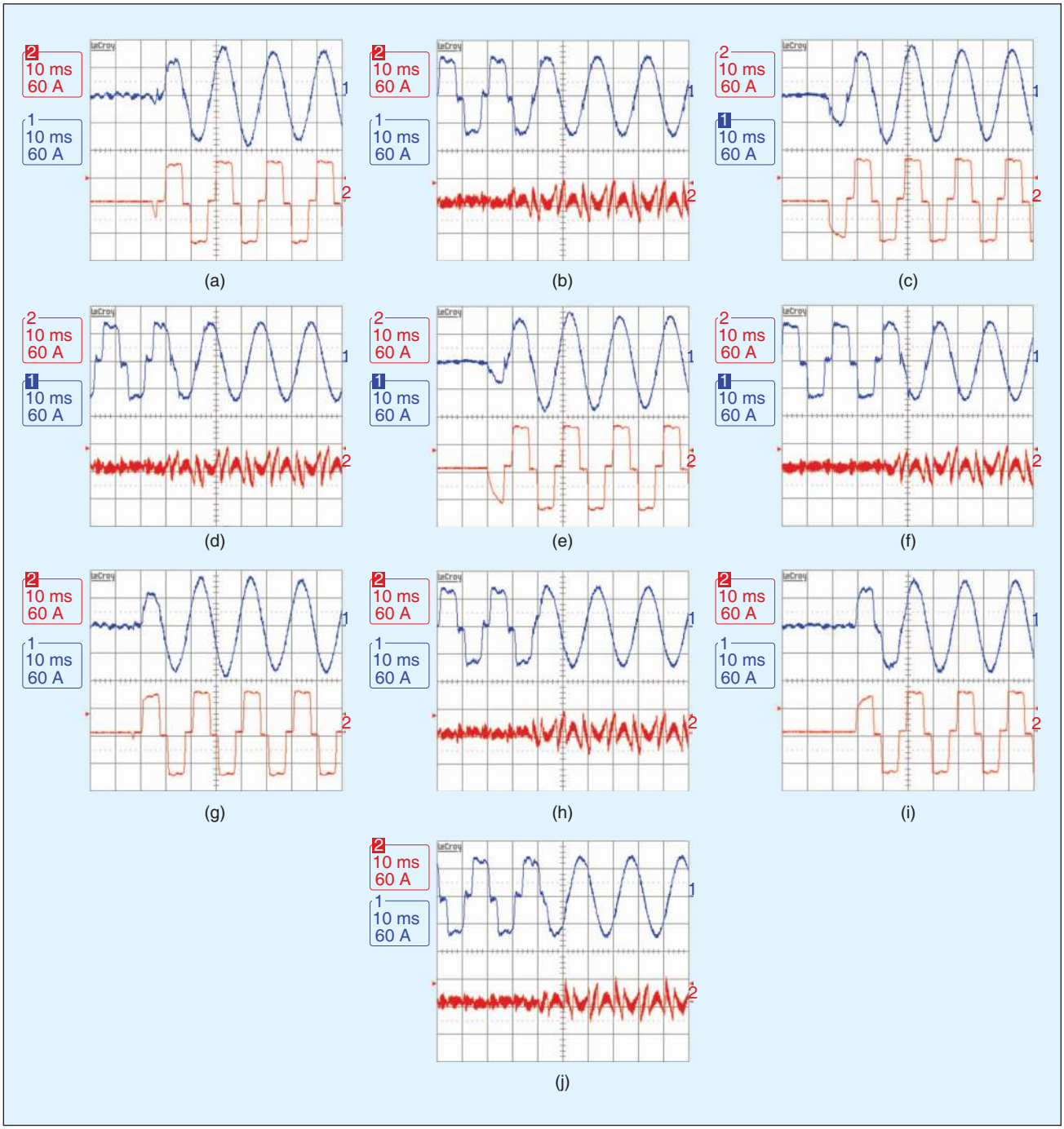

FIGURE 9 – Transient experimental results for all current controls based on selective harmonic compensation techniques. (a) APF transient performance for PI-MRI control during a load turn-on, Trace 1: i_{Sa} (A) and Trace 2: i_{La} (A). (b) APF transient performance for PI-MRI control when the harmonic compensation is enabled, Trace 1: i_{Sa} (A) and Trace 2: i_{Fa} (A). (c) APF transient performance for P-SSI control during a load turn-on, Trace 1: i_{Sa} (A) and Trace 2: i_{La} (A). (d) APF transient performance for P-SSI control when the harmonic compensation is enabled, Trace 1: i_{Sa} (A) and Trace 2: i_{Fa} (A). (e) APF transient performance for P-SSI-SRF control during a load turn-on, Trace 1: i_{Sa} (A) and Trace 2: i_{La} (A). (f) APF transient performance for P-SSI-SRF control when the harmonic compensation is enabled, Trace 1: i_{Sa} (A) and Trace 2: i_{Fa} (A). (g) APF transient performance for PI-RES control during a load turn-on, Trace 1: i_{Sa} (A) and Trace 2: i_{La} (A). (h) APF transient performance for PI-RES control when the harmonic compensation is enabled, Trace 1: i_{Sa} (A) and Trace 2: i_{Fa} (A). (i) APF transient performance for repetitive control during a load turn-on, Trace 1: i_{Sa} (A)and Trace 2: i_{La} (A). (j) APF transient performance for repetitive control when the harmonic compensation is enabled, Trace 1: i_{Sa} (A) and Trace 2: i_{Fa} (A).

Steady-State THD Performance

Some simulations have been performed to show the steady-state results of PI-SRF and DB current controllers [Figure 7(a)]. The results confirm our expectations about both techniques. Additionally, the experimental steady-state performance of the PI-SRF can be evaluated in Figure 7(b)–(d). This experimental performance corresponds with the simulation result and confirms that the performance of PI-SRF and DB current controllers is inferior to the performance of current controls based on selective harmonic compensation.

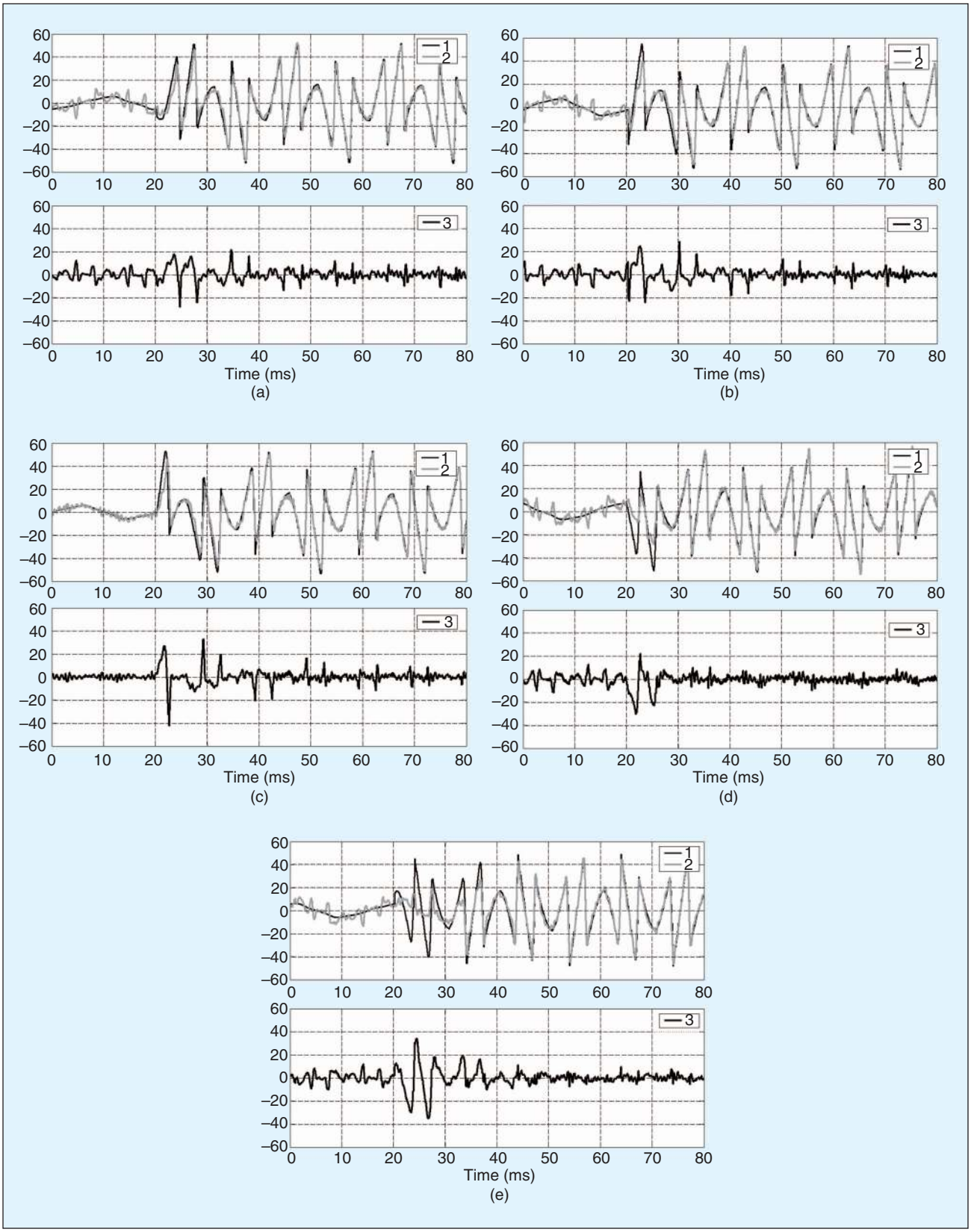

FIGURE 10 – Additional transient waveforms when harmonic compensation is enabled. (a) MRI control for α axis when harmonic compensation is enabled: 1) $i^*_{F\alpha}$ (A), 2) $i_{F\alpha}$ (A), and 3) $\epsilon_{F\alpha}$ (A). (b) P-SSI control for α axis when harmonic compensation is enabled: 1) $i^*_{F\alpha}$ (A), 2) $i_{F\alpha}$ (A), and 3) $\epsilon_{F\alpha}$ (A). (c) P-SSI-SRF control for α axis when harmonic compensation is enabled: 1) $i^*_{F\alpha}$ (A), 2) $i_{F\alpha}$ (A), and 3) $\epsilon_{F\alpha}$ (A). (d) PI-RES control for α axis when harmonic compensation is enabled: 1) $i^*_{F\alpha}$ (A), 2) $i_{F\alpha}$ (A), and 3) $\epsilon_{F\alpha}$ (A). (e) Repetitive current control for α axis when harmonic compensation is enabled: 1) $i^*_{F\alpha}$ (A), 2) $i_{F\alpha}$ (A), and 3) $\epsilon_{F\alpha}$ (A).

TABLE 3—EXECUTION TIME.

CURRENT CONTROL	EXECUTION TIME (WHOLE CONTROL)	EXECUTION TIME (CURRENT CONTROL)
PI-MRI	85 μs	28 μs
P-SSI-SRF	67 μs	20 μs
Repetitive	96 μs	49 μs

The steady-state performances of all the techniques based on selective harmonic compensation are very similar, as shown by the THD results in Table 2. For this reason, only the steady-state experimental results for the APF using the PI-MRI controller are shown in Figure 8(a) and (b). All the current controllers are stable and able to compensate up to the 25th harmonic.

A delay compensation method is required by the PI-MRI, P-SSI, P-SSI-SRF, and repetitive control starting from the 17th harmonic, while the PI-RES controller is stable.

Transient Performance

To evaluate the APF dynamic performance, two different tests have been considered. In the first case, the APF is operating, and the load is turned on and off; in the second test, the load is running, and the APF control enables and disables only the current harmonic compensation. The APF transient response for all the current controls based on selective harmonic compensation techniques is described in Figure 9(a)–(j). As the load is initially disconnected from the PCC in the load turn-on test, the transient time of the current controllers is affected by the reference generator time response. In the second transient test, the reference generator is in steady-state operation, and the transient time is due only to the current-control operation. For all the controllers, the reference current, the actual current, and the current error for the α-axis are shown in Figure 10(a)–(e). Note that the slowest response is that of the repetitive controller, while the other controllers provide similar transient performance.

Computational Burden and Design Complexity

The ease of implementation and the execution time, considered important issues for industrial applications, have also been compared. To compare the computational burden of the current controllers, the PI-MRI scheme, the P-SSI-SRF scheme, and the repetitive control scheme were implemented in a 16-b fixed-point TMS320LF2407A DSP, with a 40-MHz clock frequency. The execution times for these current-control schemes are shown in Table 3. Considering only the current-control execution time, the DSP takes 20 µs to perform the P-SSI-SRF current-control computation. Considering the PI-MRI and repetitive controls, the execution time increases to 28 µs and 49 µs, respectively. However, it is also important to consider the execution time for the whole control implementation in the case of the PI-MRI control because the computational burden is highly affected by the increased complexity of the PLL algorithm. Considering this scenario, the DSP execution times for the P-SSI-SRF, PI-MRI, and repetitive control are 67 μs, 85 μs, and 96 μs, respectively, and the P-SSI-SRF advantage increases.

Regarding the execution time for the P-SSI, it is intuitive that the complexity is more or less doubled when compared with the P-SSI-SRF. In the case of the PI-RES control, the complexity is similar to that of the P-SSI-SRF control. Considering the same number of compensated harmonics, the difference between these two current controllers regards only the delay compensation method. Considering the case presented here, in which the current controls compensate up to the 25th load current harmonic, the P-SSI-SRF needs two additional rotational transformations to perform the delay compensation method for the pairs of harmonics (17th, 19th and 23rd, 25th).

For fixed-point DSPs, the repetitive and PI-MRI current controllers are more attractive in terms of design complexity since they are implemented using the well-known FIR filter structures and integrators, respectively. In addition, the routines for an integrator, rotational transformations, or FIR filters can be easily implemented. Another important aspect concerning the repetitive control is the smaller number of parameters to be tuned.

Conclusions

We have presented a performance comparison of different DSP-based current-control techniques for shunt APFs requiring high-performance current control. The current-control solutions have been compared through simulations and experimental tests on a 25-kVA APF employing the same switching frequency (10 kHz) and the same remaining control tasks. The current controllers based on selective harmonic compensation performed better than the PI-SRF and DB controllers. With the PI-MRI, P-SSI, P-SSI-SRF, and PI-RES, increasing the number of compensated harmonics is possible but not justified, due to the controller complexity and computational burden. With the repetitive control, this complexity does not change by increasing the number of compensated harmonics. And when compared with other frequency-selective techniques, the repetitive control has a smaller number of parameters to be tuned.

The main criteria for performance evaluation are the THD of the mains line current and the transient performance for fast load variations. Concerning THD evaluation, all the frequency-selective techniques obtained good results with very similar performance. All the current controllers are stable and able to compensate up to the 25th harmonic. A delay compensation method is required by the PI-MRI, P-SSI, P-SSI-SRF, and the repetitive control starting with the 17th harmonic, while the PI-RES controller does not need delay compensation up to the 25th harmonic. The transient experimental tests show that the repetitive controller

has the slowest response, while the other controllers provide similar transient performance.

Since the performances of all the current controllers are rather similar, choosing the best solution should be strongly influenced by the ease of implementation and the execution time. In terms of fixed-point DSPs, the repetitive and PI-MRI current controllers appear to be more attractive since, as stated earlier, they are implemented using the well-known FIR filter structures and integrators, respectively. Additionally, the routines for an integrator, rotational transformations, or FIR filters can be easily obtained. In terms of code generation and execution time, however, the P-SSI-SRF and PI-RES require less code, and they are faster than the PI-MRI since they do not require multiple rotational transformations [21]. The execution time of the repetitive controller is strongly influenced by the number of coefficients N used by the FIR filter [20]; the repetitive controller implemented in our comparison has $N = 100$, resulting in an execution time higher than the other controllers.

Biographies

Leonardo Rodrigues Limongi received bachelor's and master's degrees in electrical engineering from Universidade Federal de Pernambuco in Brazil in 2004 and 2006, respectively. He then joined the Department of Electrical Engineering at the Politecnico di Torino in Italy, where he is currently pursuing a doctorate. His scientific interests include power electronics and power conditioning systems.

Radu Bojoi received a master's degree in electrical engineering from the Technical University "Gh. Asachi" of Iasi in Romania in 1993, and in 2003, he earned a doctorate from the Politecnico di Torino in Italy. From 1994 to 1999, he was an assistant professor in the Department of Electrical Drives and Industrial Automation at the Technical University of Iasi. In 2004, he joined the Department of Electrical Engineering of the Politecnico di Torino as an assistant professor. His expertise is in advanced control solutions for electrical drives and power conditioning systems, and he has published more than 40 papers in international journals and conference proceedings. He is a Member of the IEEE.

Giovanni Griva received a master's degree in electronic engineering from the Politecnico di Torino in Italy in 1990, and he earned a doctorate in 1994. From 1995 through 2001, he was an assistant professor in the department of electrical engineering at the Politecnico di Torino. Since 2002, he has been an associate professor at Politecnico di Torino. His research activity has focused on the design and development of advanced systems in the fields of power electronics, high-performance electric drives, digital control for industry applications, and power conditioning systems. He has published more than 70 papers in international conference proceedings and technical journals. He is a Member of the IEEE.

Alberto Tenconi received a master's degree and doctorate in electrical engineering from the Politecnico di Torino in Italy in 1986 and 1990, respectively. From 1988 to 1993, he was with the Electronic System Division of the FIAT Research Center. He then joined the Department of Electrical Engineering at the Politecnico di Torino, where he is currently an associate professor. His fields of interest are high-performance drive design and new power electronic device applications, and he has published more than 80 papers in international journals and international conference proceedings. He is a Member of the IEEE.

References

[1] S. Battacharya, D. M. Divan, and B. Bannerjee, "Active filter solutions for utility interface," in *Conf. Rec. IEEE ISIE*, vol. 1, 1995, pp. 53–63.

[2] S. Bhattacharya, T. M. Frank, D. M. Divan, and B. Banerjee, "Parallel active filter implementation and design issues for utility interface of adjustable speed drive systems," in *Conf. Rec. IEEE IAS'96*, vol. 2, pp. 1032–1039.

[3] H. Akagi, "New trends in active filters for power conditioning," *IEEE Trans. Ind. Applicat.*, vol. 32, no. 6, pp. 1312–1322, Nov. 1996.

[4] M. Sonnenschein, M. Weinhold, and R. Zurowski, "Shunt-connected power conditioner for improvement of power quality in distribution networks," in *Conf. Rec. Harmonics and Quality of Power (ICHQP VII)*, 1996, pp. 27–32.

[5] R. Bojoi, G. Griva, F. Profumo, M. Cesano, and L. Natale, "Shunt active power filter implementation for induction heating applications," in *Conf. Rec. IEEE APEC*, vol. 3, 2005, pp. 1674–1679.

[6] S. Buso, L. Malesani, and P. Mattavelli, "Comparison of current control techniques for active filter applications," *IEEE Trans. Ind. Electron.*, vol. 45, no. 5, pp. 722–729, Oct. 1998.

[7] M. P. Kazmierkowski and L. Malesani, "Current control techniques for three-phase voltage-source PWM converters: A survey," *IEEE Trans. Ind. Electron.*, vol. 45, no. 5, pp. 691–703, Oct. 1998.

[8] L. Malesani and P. Tomasin, "PWM current control techniques of voltage source converters—A survey," in *Conf. Rec. IEEE IECON*, vol. 2, 1993, pp. 670–675.

[9] D. G. Holmes and D. A. Martin, "Implementation of direct digital predictive current controller for single and three-phase voltage source inverters," in *Conf. Rec. IEEE IAS*, vol. 2, 1996, pp. 906–913.

[10] L. Malesani, P. Mattavelli, and S. Buso, "Robust dead-beat current control for PWM rectifiers and active filters," *IEEE Trans. Ind. Applicat.*, vol. 35, no. 3, pp. 613–620, May 1999.

[11] S. Buso, S. Fasolo, L. Malesani, and P. Mattavelli, "A dead-beat adaptive hysteresis current control," *IEEE Trans. Ind. Applicat.*, vol. 36, no. 4, pp. 1360–1367, July 2000.

[12] S. Buso, L. Malesani, P. Mattavelli, and R. Veronese, "Design and fully digital control of parallel active filters for thyristor rectifiers," in *Conf. Rec. IEEE IAS*, vol. 2, Oct. 1997, pp. 1360–1367.

[13] M. Sonnenschein and M. Weinhold, "Comparison of time-domain and frequency-domain control schemes for shunt active filters," in *Conf Rec. ETEP*, vol. 9, no. 1, pp. 5–16, Jan. 1999.

[14] M. Bojyup, P. Karlsson, M. Alakula, and L. Gertmar, "A multiple rotating integrator controller for active filters," in *Conf. Rec. EPE* [CD-ROM], 1999.

[15] P. Mattavelli and P. Tenti, "High performance active filters using selective harmonic control," in *Conf. Rec. IEEE Power Eng. Society Summer Meeting*, vol. 2, July 2000, pp. 977–982.

[16] P. Mattavelli, "A closed-loop selective harmonic compensation for active filters," *IEEE Trans. Ind. Applicat.*, vol. 37, no. 1, pp. 81–89, Feb. 2001.

[17] D. N. Zmood, D. G. Holmes, and G. Bode, "Frequency domain analysis of three phase linear current regulators," *IEEE Trans. Ind. Applicat.*, vol. 37, no. 2, pp. 601–610, Mar. 2001.

[18] D. N. Zmood and D. G. Holmes, "Stationary frame current regulation of PWM inverters with zero steady-state error," *IEEE Trans. Power Electron.*, vol. 18, no. 3, pp. 814–822, May 2003.

[19] X. Yuan, W. Merk, H. Stemmler, and J. Allmeling, "Stationary-frame generalized integrators for current control of active power filters with zero steady-state error for current harmonics of concern under unbalanced and distorted operating conditions," *IEEE Trans. Ind. Applicat.*, vol. 38, no. 2, pp. 523–532, Mar. 2002.

[20] P. Mattavelli and F. P. Marafao, "Repetitive-based control for selective harmonic compensation in active power filters," *IEEE Trans. Ind. Electron.*, vol. 51, no. 5, pp. 1018–1024, Oct. 2004.

[21] R. Bojoi, G. Griva, V. Bostan, M. Guerriero, F. Farina, and F. Profumo, "Current control strategy for power conditioners using sinusoidal signal integrators in synchronous reference frame," *IEEE Trans. Power Electron.*, vol. 20, no. 6, pp. 1402–1412, Nov. 2005.

[22] C. Lascu, L. Asiminoaei, I. Boldea, and F. Blaabjerg, "High performance current controller for selective harmonic compensation in active power filters," *IEEE Trans. Power Electron.*, vol. 22, no. 5, pp. 1826–1835, 2007.